

## Elements of a dielectric laser accelerator

JOSHUA MCNEUR,<sup>1</sup> MARTIN KOZÁK,<sup>1</sup> NORBERT SCHÖNENBERGER,<sup>1</sup> KENNETH J. LEEDLE,<sup>2</sup> HUIYANG DENG,<sup>2</sup> ANDREW CEBALLOS,<sup>2</sup> HEINAR HOOGLAND,<sup>3</sup> AXEL RUEHL,<sup>4,5</sup> INGMAR HARTL,<sup>6</sup> RONALD HOLZWARTH,<sup>3</sup> OLAV SOLGAARD,<sup>2</sup> JAMES S. HARRIS,<sup>2,7</sup> ROBERT L. BYER,<sup>2,7</sup> AND PETER HOMMELHOFF<sup>1,8,\*</sup>

<sup>1</sup>Department of Physics, Friedrich-Alexander-Universität Erlangen-Nürnberg, 91058 Erlangen, Germany

<sup>2</sup>Department of Electrical Engineering, Stanford University, Stanford, California 94305, USA

<sup>3</sup>Menlo Systems GmbH, Am Klopferspitz 19a, 82152 Martinsried, Germany

<sup>4</sup>Leibniz University Hannover, QUEST-Leibniz-Research School, Institute for Quantum Optics, 30167 Hannover, Germany

<sup>5</sup>Laser Zentrum Hannover e.V., 30419 Hannover, Germany

<sup>6</sup>Deutsches Elektronen-Synchrotron DESY, 22607 Hamburg, Germany

<sup>7</sup>Department of Applied Physics, Stanford University, Stanford, California 94305, USA

<sup>8</sup>Max-Planck-Institute for the Science of Light, 91058 Erlangen, Germany

\*Corresponding author: peter.hommelhoff@physik.uni-erlangen.de

Received 16 February 2018; revised 11 April 2018; accepted 12 April 2018 (Doc. ID 323387); published 25 May 2018

We experimentally demonstrate several physical concepts necessary for the future development of dielectric laser accelerators—photonic elements that utilize the inelastic interaction between electrons and the optical near fields of laser-illuminated periodic nanostructures. To build a fully photonic accelerator, concatenation of elements, large energy gains, and beam steering elements are required. Staged acceleration is shown using two spatio-temporally separated interaction regions. Further, a chirped silicon grating is used to overcome the velocity dephasing of subrelativistic electrons with respect to its optical near fields, and last, a parabolic grating geometry serves for focusing of the electron beam. © 2018 Optical Society of America under the terms of the OSA Open Access Publishing Agreement

**OCIS codes:** (230.1150) All-optical devices; (230.3990) Micro-optical devices; (320.0320) Ultrafast optics; (350.4238) Nanophotonics and photonic crystals.

<https://doi.org/10.1364/OPTICA.5.000687>

The widespread use of high-energy particle beams in basic research [1,2], medicine [3], and coherent x-ray generation [4] combined with the large size of modern radio frequency (RF) accelerator devices and facilities has motivated a strong interest in smaller-footprint accelerators operating in regimes outside of RF [5]. Working at optical frequencies, dielectric laser accelerators (DLAs)—transparent laser-driven nanoscale dielectric structures whose near fields can synchronously accelerate charged particles—have demonstrated high-gradient acceleration with a variety of laser wavelengths, materials, and electron beam parameters [5–10]. Similar to novel laser-assisted electron microscopy techniques such as photon-induced near-field electron microscopy (PINEM) [11], the acceleration of electrons in DLAs depends on their inelastic interactions with the optical near fields

at laser-illuminated nanostructures. However, the interaction time between the electrons and photons and thus the final energy and momentum change of the electrons is strongly enhanced in DLAs. Dielectric laser acceleration is thus clearly a field-driven interaction whose description falls beyond perturbation theory (the maximum energy gain observed here corresponds to an absorption of 4000 driving photons). We thus employ a classical treatment: the spatial distribution of the optical near fields of DLAs can be Fourier decomposed into a set of spatial harmonics propagating along the surface of the nanostructure with different phase velocities. Synchronous interaction between the electrons and one of the harmonics occurs when the phase velocity of a particular harmonic,  $v_{\text{ph,acc}}$ , matches the velocity of electrons traveling parallel to the mode, i.e.,  $v_{\text{ph,acc}} = \frac{\omega}{k_{\parallel\text{acc}}} = v$ .

Here,  $\omega$  is the angular frequency of the driving field,  $v$  is the velocity of the electrons, and  $k_{\parallel\text{acc}}$  is the longitudinal component (in the electron beam direction) of the wave vector of the synchronous spatial harmonic (see Fig. 1). In the case of the DLA geometries described below, the force on the electrons (in the electron coordinate system) due to interaction with this mode is [12]

$$F_{r'} = q * e^{\frac{-i\omega y'}{\tilde{\gamma}\beta c} + i\left(\frac{\omega z'}{\beta c} - \omega t + \theta\right)} * \begin{bmatrix} (-icB_x \tan \alpha)/(\beta\tilde{\gamma}) - E_x \sin \alpha \tan \alpha \\ (-cB_x)/(\beta\tilde{\gamma}^2) + (iE_x \tan \alpha)/\tilde{\gamma} \\ (icB_x)/(\beta\tilde{\gamma}) + E_x \sin \alpha \end{bmatrix}. \quad (1)$$

Here,  $y'$  and  $z'$  are coordinates with respect to the electron beam propagation axis,  $c$  is the speed of light,  $t$  is time,  $q$  is the charge of an electron,  $\beta = v/c$ ,  $\alpha$  is the angle between the electrons and the grating teeth,  $\tilde{\beta} = \beta \cos \alpha$ ,  $\tilde{\gamma} = (1 - \beta^2)^{-1/2}$ ,  $\tilde{\gamma} = (1 - \tilde{\beta}^2)^{-1/2}$ , and  $B_x$  ( $E_x$ ) is the amplitude of the magnetic (electric) field perpendicular to the grating vector, determined numerically for the transverse magnetic (transverse electric) mode independently. Equation (1) has three important consequences. First, the exerted force depends on the relative phase  $\theta$  between the electrons and the accelerating mode. Second, synchronous

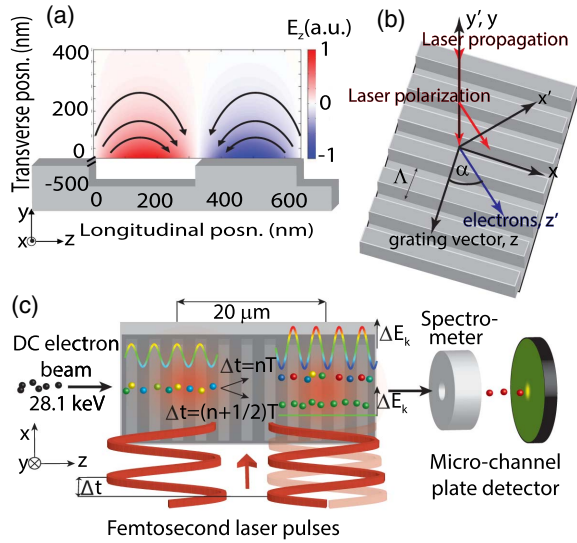


**Fig. 1.** (a) Longitudinal fields of the accelerating mode excited at a transparent dielectric grating illuminated parallel to the  $y$  direction. Arrows indicate the electromagnetic forces for positively charged particles. Note that acceleration, deceleration, and deflection can occur depending on the electron injection phase  $\theta$ . (b) Geometry of the DC electron beam passing (with an angle  $\alpha$ ) by perpendicularly illuminated grating teeth. (c) Electron beam (electrons indicated by spheres) interacts with two consecutive laser pulses (red curves). The energy modulation of electrons during interaction with the first laser pulse (visualized by color scale) can be either doubled (when  $\Delta t = nT$ ) or suppressed ( $\Delta t = (n + 1/2)T$ ) by the second pulse.

acceleration relies on the velocity of the accelerating mode matching the increasing electron velocity (without changing the accelerating mode velocity; accelerated electrons injected on the crest will soon slip forward towards decelerating phases). The force of the synchronous mode on traversing electrons for  $E_x = \alpha = 0$  is illustrated in Fig. 1(a). Third, there are significant deflecting forces in the  $x'$  and  $y'$  directions, strongly influencing the electron dynamics.

For all subrelativistic DLA experiments to date, single stage acceleration has been demonstrated with interaction lengths less than  $10 \mu\text{m}$  [8–10]. To realize many of the applications that this technology enables, e.g., miniaturized MeV electron sources and table-top coherent x-ray sources [5], the interaction length must exceed 1 mm, and thus, the above properties of the interaction must be addressed via the design of DLAs. Here, we demonstrate critical developments necessary towards this end. By creating two interaction regions via illumination of a nanograting with two spatio-temporally separated laser pulses, we demonstrate phase control of the accelerating fields with the attosecond precision necessitated by the optical driving frequency. This leads to a doubling of the maximum electron energy gain from 0.75 keV to 1.3 keV, corresponding to an energy modulation of 2.5% to 5% of the initial beam energy. Further, a chirped grating geometry is utilized to match the phase velocity of the accelerating mode to the increasing electron velocity. Here, the energy gain reaches 10% of the initial electron energy. Last, optically driven transverse focusing of a subset of an electron beam with focal lengths below  $200 \mu\text{m}$  is achieved via a parabolic grating geometry.

Two-stage phase-controlled acceleration is demonstrated here with the experimental setup shown in Fig. 1(c). Femtosecond

laser pulses generated either in thulium- or thulium-holmium-doped fiber lasers operating at wavelengths of  $1.93 \mu\text{m}$  and  $2.05 \mu\text{m}$  (pulse durations of 600 fs and 380 fs, respectively) generate two acceleration regions after passing through a Mach-Zehnder-type interferometer ([13], see Supplement 1). We note that an operating wavelength of approximately  $2 \mu\text{m}$  was chosen as a compromise between the transverse decay length of the optical near field,  $\delta = \lambda\beta\gamma/2\pi$  and the long-wavelength limit of the available energy efficient amplified femtosecond laser sources. A spatial separation between the centers of the two accelerating regions on the Si grating ( $d = 18 \pm 2 \mu\text{m}$ ) is reached by using a noncollinear geometry for the output beams from this interferometer. A DC electron beam with an initial energy of  $E_{k0} = 28.1 \text{ keV}$  passes parallel to the surface of a rectangular Si grating with a period of 620 nm, a tooth width of 340 nm, and a tooth depth of 450 nm [optimized in numerical studies (see Supplement 1)]. In both interaction regions,  $\alpha = E_x = 0$ . After the interaction, electrons are spectrally filtered by a retard-field spectrometer that transmits only electrons with a kinetic energy higher than the applied potential barrier ( $E_k > qU_s$ , where  $U_s$  is the DC voltage applied to the spectrometer). The transmitted electrons are detected by a Chevron type micro-channel plate (MCP) detector ([8,14], see Supplement 1).

In Fig. 2(a) we show the dependence of the accelerated electron current on the relative phase  $\Delta\theta = 2\pi\Delta t/T$  of the two laser pulses measured in the temporal window  $\Delta t = 175\text{--}205 \text{ fs}$  (the electron travel time between the centers of the two interaction regions is  $t_{tr} = 190 \pm 10 \text{ fs}$ ), with  $T = 6.5 \text{ fs}$  the optical period and  $\Delta t$  the temporal difference in arrival time of the two pulses. The current of electrons with energy gains higher than 400 eV (squares) is displayed along with numerical results (red curve). For a phase difference of  $\Delta\theta = \pm 2\pi n$  ( $n$  an integer), energy modulation is most effective in the two acceleration regions, whereas at  $\Delta\theta = \pi \pm 2\pi n$ , the energy modulation imparted to electrons in one region is negated in the second.

The crucial property of multi-stage acceleration is that the increase of the energy gain of a subset of electrons traversing multiple interaction regions exceeds the energy gain provided by a single interaction region illuminated by a laser pulse at maximum intensity (determined by the laser-induced damage threshold of the DLA material). Figure 2(b) shows the accelerated electron current as a function of the minimum energy gain for the relative phase differences  $\Delta\theta = \pm 2\pi n$  (red squares) and  $\Delta\theta = \pi \pm 2\pi n$  (black circles) between the two laser pulses.

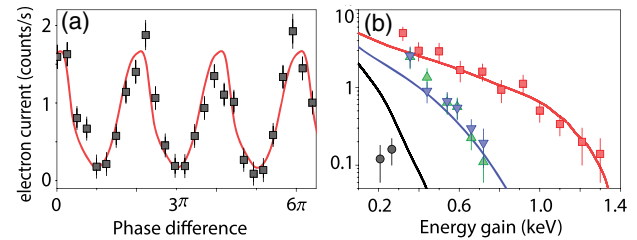


**Fig. 2.** (a) Dependence of the accelerated electron current on the relative phase between the two driving optical pulses for a minimum energy gain of 400 eV (black squares) along with numerical results. (b) Accelerated electron count rate as a function of the minimum energy gain for  $\Delta\theta = 0$  (red squares),  $\Delta\theta = \pi$  (black circles), and for acceleration by each individual laser pulse (green and blue triangles) compared to the numerical results (lines).

We further show the integrated electron energy spectra in each individual interaction region operating at maximal intensity. The peak laser fluence in each region is  $0.13 \text{ J/cm}^2$ , directly below the measured damage fluence of  $0.14 \text{ J/cm}^2$ . The maximum energy gain of  $750 \text{ eV}$  for electrons interacting with each section individually (blue and green triangles) is almost doubled to an energy gain of  $1.3 \text{ keV}$  when electrons interact with both pulses at the ideal phase difference. However, we do not observe an exactly doubled energy gain of  $1.5 \text{ keV}$  due to deflection of electrons away from or towards the surface of the structure, dephasing of electrons with significantly increasing velocities, and the electronic noise of our detection system. This result demonstrates the critical ability to increase the total energy gain in a photonic accelerator by using multiple phase-controlled DLA stages.

DLA-based applications that require a miniaturized device require a miniaturized cathode and thus limit the injected electron energy to tens of keV [15]. Hence, the electron beam needs to be bunched and pre-accelerated at subrelativistic energies. The former occurs naturally in DLAs due to the induced velocity distribution on the electron beam (see Supplement 1). The latter must take into account the velocity dephasing of accelerated electrons with respect to the accelerating mode. Subrelativistic electrons injected at accelerating phases have rapidly increasing velocities, leading to dephasing between the optical mode and electron beam. The increasing electron velocity can be compensated for by either frequency chirping the incident laser pulse or modifying the acceleration structure design to match the phase velocity of the accelerating mode to the design particle velocity at all longitudinal coordinates. Since the former is limited by the spectral width of the laser pulse, here we use lithography-based structural chirping of the grating instead.

In this design, the distance between grating teeth depends linearly on the longitudinal coordinate  $z$  as  $\lambda_p = \lambda_{p0} + az$ , where  $\lambda_{p0} = 620 \text{ nm}$  is the starting grating period and  $a$  the chirp parameter. In Fig. 3 we show the accelerated electron current as a function of  $qU_s - E_{k0}$  for different values of  $a$  but the same laser parameters. Without any structural chirp ( $a = 0$ ), dephasing limits the maximum achievable energy gain to  $\Delta E_k = 0.76 \text{ keV}$ . For  $a = 6.5 \times 10^{-4}$ , the maximum energy gain is more than tripled to  $\Delta E_k = 2.6 \text{ keV}$ , corresponding to a peak acceleration gradient of  $69 \text{ MeV/m}$ . We have thus experimentally demonstrated a means to overcome the velocity dephasing limit.

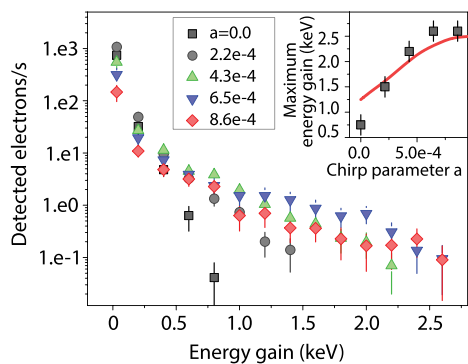


**Fig. 3.** Accelerated electron count rate as a function of minimum energy gain for different values of the chirp parameter  $a$ . Inset: maximum energy gain as a function of  $a$  (points) compared to numerical results (red curve).

The maximum energy gain is now limited by the incident field amplitude of  $E_{\max} = 1.3 \text{ GV/m}$ , the interaction distance, which in turn is given by the laser spot radius  $w = 29 \pm 3 \mu\text{m}$ , and critically, deflection of electrons away from or towards the surface of the grating due to their interaction with the transverse electric and magnetic fields [see Eq. (1)].

In order to control the transverse dynamics of electrons traversing DLA structures, we employ the focusing structure presented in Fig. 4(a). In contrast with conventional magnetic focusing elements (e.g., solenoids), this laser-illuminated photonic element lends itself towards miniaturization and straight-forward integration with other DLA elements. A deflecting mode is locally excited at a grating tilted by an angle with respect to the electron beam and laser polarization. For small angles  $\alpha$ , Eq. (1) indicates that, to lowest order in  $\alpha$ , the magnitude of the deflection force in the  $x'$  direction is  $|F_{x'}| \approx qcaB_x/(\beta\gamma)$ . Thus, focusing in  $x'$  can be achieved by curving the grating teeth with an angle that depends on the distance from the design axis as  $\alpha = \sigma s$ . Here,  $\sigma$  is a constant, and  $s$  is the distance from the design axis of electron propagation. This leads to parabolically shaped grating teeth [see Fig. 4(a) and Supplement 1].

We demonstrate DLA-induced focusing by measurement of the mean accelerated electron deflection angle  $\phi$  as a function

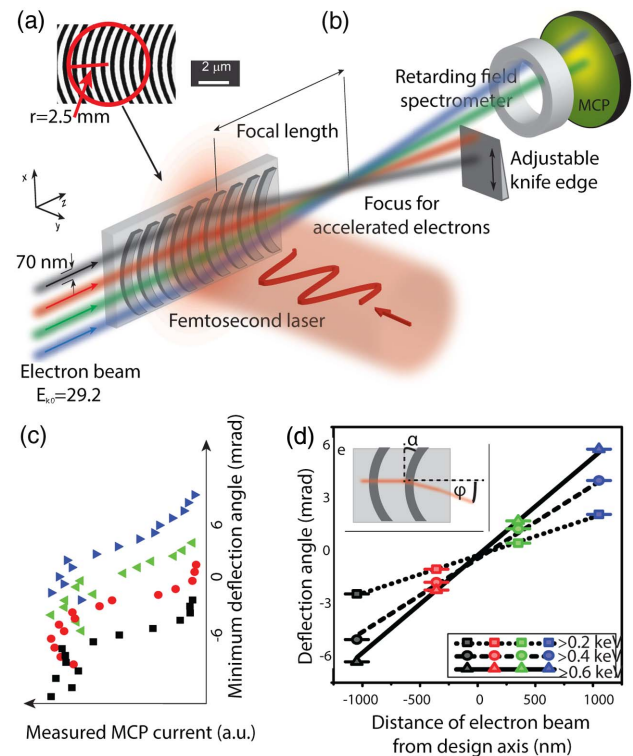


**Fig. 4.** (a) Scanning electron microscope image of the focusing element fabricated from Si. The radius of curvature at the vertex of the parabola is  $2.5 \mu\text{m}$ . (b) Accelerated electrons that traverse the lens structure above (in  $x$ ) the parabolic vertex are deflected downwards, and those that traverse below the vertex are deflected upwards. The grating curvature angle  $\alpha$  and electron beam deflection angle  $\phi$  are shown in the inset (e). Spatial profile of the accelerated electrons as a function of  $x$  is measured with a knife edge scan (see Supplement 1), sample results of which are shown in (c). (d) Position of the centroid of the accelerated spatial distribution at the location of the knife edge as a function of electron beam position on the structure  $x$ , with linear fits for each minimum energy gain setting.



of the position of the electron beam center  $x$  within the interaction region [see Fig. 4(b) and Supplement 1]. We observe a linear dependence  $\phi = bx$ , with the coefficient  $b$  corresponding to the inverse of the focal length  $f$ . Because the synchronous mode simultaneously deflects and accelerates in this structure [16], the focal distance differs for electrons with different energy gains [different colors in Fig. 4(d)]. We find that the effective focal lengths of electrons with minimum energy gains of 200 eV, 400 eV, and 600 eV are  $500 \pm 20$ ,  $260 \pm 10$ , and  $190 \pm 10$   $\mu\text{m}$ , respectively for  $\sigma = 0.39$   $\text{rad } \mu\text{m}^{-1}$ . Such strong focusing is not possible at this scale using traditional focusing elements. Further, in Eq. (1), it is apparent that phases  $\theta$  that are strongly focusing are also strongly accelerating, explaining the dependence of the effective focal length on the minimum measured energy gain. However, further attention must be paid to focusing in the  $y'$  direction due to the  $\pi/2$  phase shift of  $F_{y'}$  with respect to  $F_{x'}$  [see Eq. (1)]. Alternating focusing elements in  $y'$  and  $x'$  may be used in a similar manner to a so-called FODO scheme (a lattice with focusing-propagation-defocusing-propagation elements in one transverse direction and defocusing-propagation-focusing-propagation elements in the other) to achieve focusing simultaneously in both axes.

To summarize, we have designed and experimentally demonstrated several critical components of a 2  $\mu\text{m}$  fiber laser-based DLA. Note that for relativistic electrons ( $>5$  MeV), high damage threshold material [17] (e.g.,  $\text{CaF}_2$ ), and identical laser parameters, the expected acceleration gradient scales favorably to 1.2 GeV/m due to the more efficient coupling of laser light into the appropriate longitudinal modes (see Supplement 1). Further, much higher energy gains will be achieved through additional stages, the foundation of which we have demonstrated here, namely, staged acceleration, chirped elements to circumvent dephasing, and focusing elements. The principle questions that remain include the incorporation of an electron source appropriate for DLA operation [15,18], demonstration and incorporation of microbunching elements, and integration of the elements already demonstrated. Closely tied to the source, the electron current that can be supported in such a structure depends on Coulomb repulsion [12], the incident laser profile, and the electron-generated wakefields, requiring involved numerical investigation outside the scope of this Letter. Nevertheless, the linear scaling of the average current with the repetition rate of the incident laser beam is promising due to the commercial availability of power-efficient high-repetition-rate femtosecond (fiber) lasers.

**Funding.** Gordon and Betty Moore Foundation; Bundesministerium für Bildung und Forschung (BMBF) (05K16WEC); H2020 European Research Council (ERC); Eurostars (E! 6698).

**Acknowledgment.** J. M. and M. K. contributed equally to this work.

See Supplement 1 for supporting content.

## REFERENCES

1. E. L. Ginzton, W. W. Hansen, and R. W. Kennedy, *Rev. Sci. Instrum.* **19**, 89 (1948).
2. J. C. Nygard and R. F. Post, *Nucl. Instrum. Methods* **11**, 126 (1961).
3. R. R. Wilson, *Radiology* **47**, 487 (1946).
4. B. W. J. McNeil and N. R. Thompson, *Nat. Photonics* **4**, 814 (2010).
5. R. J. England, R. J. Noble, K. Bane, D. H. Dowell, C. Ng, J. E. Spencer, S. Tantawi, Z. Wu, R. L. Byer, E. Peralta, K. Soong, C. Chang, B. Montazeri, S. J. Wolf, B. Cowan, J. Dawson, W. Gai, P. Hommelhoff, Y. Huang, C. Jing, C. McGuinness, R. B. Palmer, B. Naranjo, J. Rosenzweig, G. Travish, A. Mizrahi, L. Schachter, C. Sears, G. R. Werner, and R. B. Yoder, *Rev. Mod. Phys.* **86**, 1337 (2014).
6. E. A. Peralta, K. Soong, R. J. England, E. R. Colby, Z. Wu, B. Montazeri, C. McGuinness, J. McNeur, K. J. Leedle, D. Walz, E. B. Sozer, B. Cowan, B. Schwartz, G. Travish, and R. L. Byer, *Nature* **503**, 91 (2013).
7. K. P. Wootton, Z. Wu, B. M. Cowan, A. Hanuka, I. V. Makasyuk, E. A. Peralta, K. Soong, R. L. Byer, and R. J. England, *Opt. Lett.* **41**, 2696 (2016).
8. J. Breuer and P. Hommelhoff, *Phys. Rev. Lett.* **111**, 134803 (2013).
9. K. J. Leedle, R. F. Pease, R. L. Byer, and J. S. Harris, *Optica* **2**, 158 (2015).
10. K. J. Leedle, A. Ceballos, H. Deng, O. Solgaard, R. F. Pease, R. L. Byer, and J. S. Harris, *Opt. Lett.* **40**, 4344 (2015).
11. B. Barwick, D. J. Flannigan, and A. H. Zewail, *Nature* **462**, 902 (2009).
12. J. Breuer, J. McNeur, and P. Hommelhoff, *J. Phys. B* **47**, 234004 (2014).
13. M. Kozák, J. McNeur, K. J. Leedle, N. Schönenberger, A. Ruehl, I. Hartl, J. S. Harris, R. L. Byer, and P. Hommelhoff, *Nat. Commun.* **8**, 14342 (2017).
14. J. Breuer, R. Graf, A. Apolonski, and P. Hommelhoff, *Phys. Rev. Spec. Top. Accel. Beams* **17**, 021301 (2014).
15. J. McNeur, M. Kozák, D. Ehberger, N. Schönenberger, A. Tafel, A. Li, and P. Hommelhoff, *J. Phys. B* **49**, 034006 (2016).
16. T. Plettner and R. L. Byer, *Phys. Rev. Spec. Top. Accel. Beams* **11**, 030704 (2008).
17. L. Gallais, D.-B. Dotti, M. Commandré, G. Batavičute, E. Pupka, M. Sciuka, L. Smalakys, V. Sirutkaitis, and A. Melninkaitis, *J. Appl. Phys.* **117**, 223103 (2015).
18. J. Hoffrogge, J. P. Stein, M. Krüger, M. Förster, J. Hammer, D. Ehberger, P. Baum, and P. Hommelhoff, *J. Appl. Phys.* **115**, 094506 (2014).